

# Counter-rotation of magnetic beads in spinning fields

Jean Farago, Thierry Charitat, Alexandre Bigot, Romain Schotter, and Igor Kulic  
*Université de Strasbourg, CNRS, Institut Charles Sadron UPR-22, Strasbourg, France*

(Dated: May 15, 2022)

A magnetized bead in a magnetic field seeks to minimize its magnetic free energy by aligning its magnetic moment with the field direction and by moving towards the maximum of the field's intensity. However, when the bead is coupled to a substrate it is forced to roll. The two otherwise independent degrees of freedom, translation and rotation, become tightly coupled giving rise to subtle and often counterintuitive effects. Here we investigate one such, easily reproducible, yet stunning effect : A neodymium bead placed on top of a laboratory magnetic stirrer. When the stirrer's magnet spins at slow rates the bead naturally follows the field. However, surprisingly, at high spinning rates the bead suddenly inverts its direction and runs, to the surprise of the observer, in the opposite direction, against the driving field direction. This effect, experimentally investigated in [*J. Magn. Magn. Matter*, **476**, 376-381, (2019)], is here comprehensively studied, with numerical simulations and a theoretical approach complementing experimental observations.

## I. INTRODUCTION

The broad availability of magnetic neodymium beads has led to an increased "table top" experimental interest in their self-assembly and individual dynamics [1–4]. Merely rolling such a bead on the top of the table leads to surprisingly complex behavior, with bead trajectories that depend on the motion speed and inclination to the local earth magnetic field [5]. In the microscopic realm, the interaction of ferro- and superparamagnetic beads with external fields and surface confinement has been extensively investigated. Spatially inhomogeneous, dynamic magnetic fields that are linearly propagating [6] or rotationally spinning [3, 7] along surfaces have been investigated. The confinement of magnetic or magnetizable objects to solid [3, 6] and fluid interfaces [8, 9] under oscillating fields leads to an intricate phenomenology including self-assembly and self-propulsion [10].

A permanently magnetized object placed in a non-uniform field, moves to minimize its magnetic free energy via two mechanisms: a) By aligning its magnetic moment with the field direction and b) by moving towards the maximum of field intensity. However, when coupled to a substrate the two otherwise independent degrees of freedom become tightly coupled giving rise to subtle and often counterintuitive effects. Here we investigate one such easily reproducible, yet stunning effect : A neodymium bead placed on top of a laboratory magnetic stirrer. When the stirrer's magnet rotates at slow rates the bead naturally follows the field. However, surprisingly, once the field rotates fast enough the bead inverts its direction and rolls, to the surprise of the observer, in the opposite direction - against the driving field direction. This effect was recently described by Chau et al. [11] and in a related form by Gissinger [7].

In this paper, we revisit the experiments of Chau et al. [11] with a comprehensive approach which combines experiments, numerical simulations and theo-

retical analysis. The benefit of numerical simulations is to provide a complete description of the internal motion of the beads, which are quite complicated to access experimentally. We performed experiments, rather similar to the "opposite polarity case" described in [11], but simpler as we used an usual magnetic stirrer (commonly found in chemical laboratories) to provide the rotating magnetic field. We then wrote down the dynamical equations of a magnetic bead moving on the horizontal plane of the stirrer, assuming a viscous friction between the bead and the stirrer. The features of the magnetic field of the stirrer have been carefully modeled, in order to reproduce as faithfully as possible the experiments. We simulated the dynamical equations obtained and by fitting two parameters of the model, we were able to reproduce qualitatively and quantitatively our experimental results. A theoretical analysis of the motion allows us (i) to understand the radial stabilization of the bead in its counter-rotating motion, (ii) to confirm the asymptotic role of the free rolling at large driving angular velocities, and (iii) to show that counter-rotating motion is not possible when purely paramagnetic beads (without remanent magnetization) are used.

The paper is organized as follows. In sections II and III, the system is introduced and our experimental results are presented. The dynamical equations of the system and the modeling of the rotating magnetic field are derived in section IV. Two typical motions are then discussed in detail in section V. A theoretical discussion follows in section VI. For the sake of completeness, equations for the internal dynamics of the bead in spherical coordinates are reported in Appendix .

## II. DESCRIPTION OF THE SYSTEM

The system, depicted in fig. 1, is a ferromagnetic (neodymium) sphere of mass  $m = 0.5$  g, radius

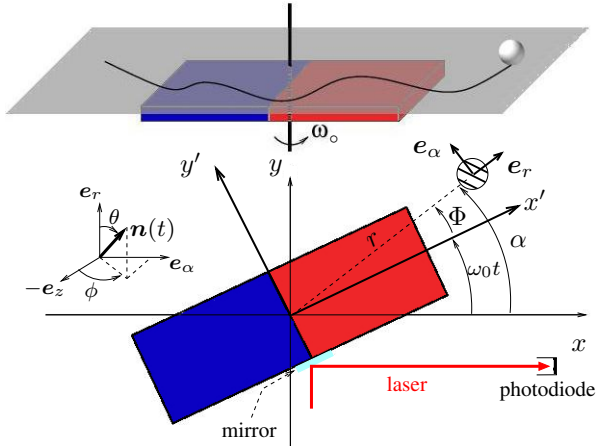


FIG. 1. Sketch of the system and the main notations used throughout the paper.  $\theta$  and  $\phi$  are used to orient the magnetic axis  $\mathbf{n}$  of the bead :  $\mathbf{n} = \cos(\theta)\mathbf{e}_r + \sin(\theta)(\sin(\phi)\mathbf{e}_\alpha - \cos(\phi)\mathbf{e}_z)$ .

$R = 2.5$  mm and magnetic moment along a diameter  $\mu(t) = \mu\mathbf{n}(t)$  (with  $\mathbf{n}(t)$  a unit vector going from the south pole of the magnet to the north pole), placed on the stirrer surface (substrate). The latter is immobile in the laboratory frame ( $O, \mathbf{e}_x, \mathbf{e}_y, \mathbf{e}_z$ ) and located at the height  $z = 0$ . The position of the sphere is described by a two-dimensional vector  $\mathbf{r}_0 = x_0\mathbf{e}_x + y_0\mathbf{e}_y = r_0\mathbf{e}_r$ , its vertical coordinate staying at  $z_0 = R$ . In the following, the local polar vector basis is denoted by  $(\mathbf{e}_r, \mathbf{e}_\alpha)$  and the corresponding cylindrical coordinates by  $(r_0, \alpha_0, z_0)$ .

Below the substrate, at the coordinate  $z_0 = -h_m = -16.2$  mm, a permanent magnet, of approximately rectangular shape (with a length  $2\ell_m = 56$  mm, a width  $w_m = 40$  mm, and thickness 9 mm), rotates counterclockwise around the axis  $Oz$  with a constant angular speed  $\omega_0$ . Its time-dependent magnetic field  $\mathbf{B}$  influences the spherical bead via the interaction potential  $V(\mathbf{n}, \mathbf{r}_0, t) = -\mu\mathbf{n} \cdot \mathbf{B}(x_0, y_0, R, t)$ . Notice that this interaction potential is an approximation which assumes that the magnetic field can be considered constant over the volume of the sphere.

### III. EXPERIMENTAL RESULTS

We recorded the bead trajectories using a high-speed camera (Phantom Miro LC320S) at 200 fps, and extracted them using the tracking features of the open-source software Blender, see fig. 2 [12]. We used the reflection of a laser beam on a mirror glued on the rotating magnet (cf. fig. 1) to measure precisely the rotating frequency  $\omega_0$ .

At very low rotation frequencies, the bead is trapped above one of the two poles of the rotating

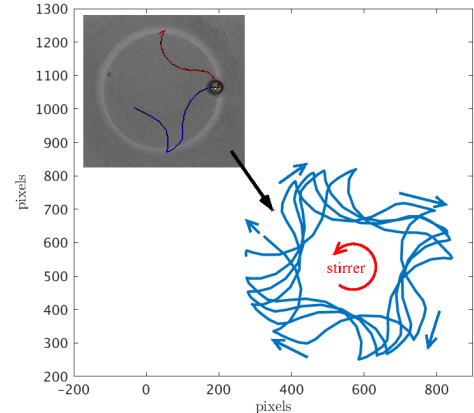


FIG. 2. Example of a counter-rotating trajectory tracked by Blender. The frequency of the rotating magnet is  $\omega_0/2\pi = 10.7$  Hz.

magnet (where the accessible magnetic field is maximum), and the bead's motion is trivially a corotation at the same angular speed as the rotating magnet. The internal rotation of the magnet is largely dictated by the requirement that the bead axis stays parallel to the local magnetic field. This internal motion yields a substantial friction between the bead and the horizontal slab of the stirrer. Beyond a certain angular velocity  $\omega_c$ , the friction force is too high and the bead is no longer trapped in the magnetic potential. The typical value of  $\omega_c$  is obtained by balancing the friction force  $m\gamma R\omega_c$  with the magnetic force at stake  $\mu B/\ell$ . We get  $\omega_c \simeq \mu B/[\gamma R\ell]$ . Fed with typical numerical values of our experiment (see values given above and in section IV A), we obtain  $\omega_c/(2\pi) \simeq 7$  Hz, which is in accordance with what we observed in our experiment. For frequencies slightly above this limiting value, the behaviour is complex, mainly chaotic. This window is however rather narrow, and as can be seen in fig. 2 for  $\omega_c/(2\pi) \simeq 10$  Hz, a regular regime (with some precession) sets in, where the global motion of the bead is counter-rotating, with a pattern, whose amplitude is large at small frequencies and shrinks at higher frequencies (see fig. 9, which corresponds to  $\omega_0/(2\pi) = 19.9$  Hz. We term these patterns “festoons” in the following because of their similarity with the garland-like adornment of some architectural friezes [13].

We measured as a function of the magnet rotation angular frequency  $\omega_0$  (i) the mean radius  $r_0$  of the trajectories (ii) its standard deviation  $\delta r_0 = \sqrt{\langle r_0^2 \rangle - \langle r_0 \rangle^2}$  and (iii) the mean angular velocity  $\dot{\alpha}_0$  of the bead.

The mean radius and standard deviations are shown in fig. 3. The large standard deviation at small frequencies come from the large festooning of the trajec-

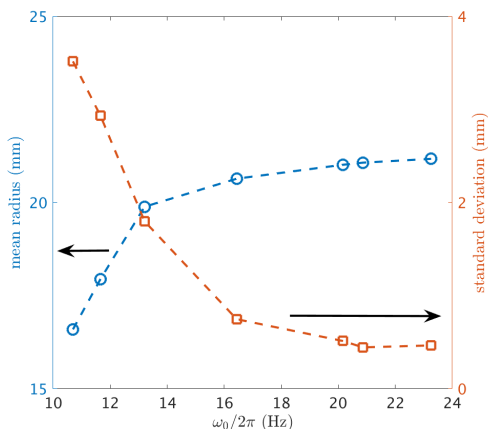


FIG. 3. Blue circles : Mean radius  $\langle r_0 \rangle$  of the trajectory (left plot). Red squares : Standard deviation  $\sqrt{\langle r_0^2 \rangle - \langle r_0 \rangle^2}$  (right plot). Both curves are plotted as a function of the magnet frequency  $\omega_0/2\pi$ . Only the counter-rotative regime is shown. The dashed lines are a guide for the eye.

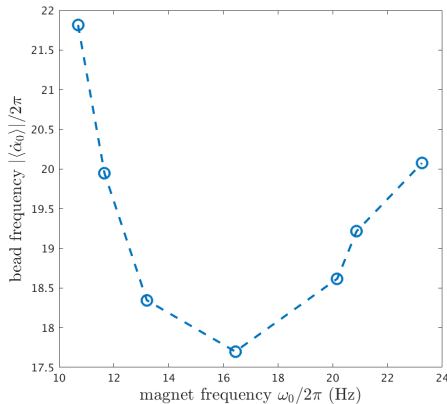


FIG. 4. Mean bead frequency  $|\langle \dot{\alpha}_0 \rangle|/2\pi$  as a function of the magnet frequency  $\omega_0/2\pi$ . Notice that  $\langle \dot{\alpha}_0 \rangle$  is everywhere negative because the regime studied is exclusively counter-rotating. The dashed line is a guide for the eye.

tory, as can be seen in the example of fig. 2. When the frequencies become too small, the festoons cannot grow indefinitely and a chaotic behaviour is instead observed (for still lower frequencies, a co-rotative

locked motion is recovered). At larger frequencies, the festoons are still present, but with smaller amplitudes.

In fig. 4 we plot the (absolute value of the) revolution frequency of the bead  $|\langle \dot{\alpha}_0 \rangle|/2\pi$  against the magnet frequency  $\omega_0/2\pi$ . The typical values of  $|\dot{\alpha}_0|$  are one order of magnitude smaller than  $\omega_0$ , which is qualitatively explained by the mechanism which allows the counter-rotation : On the one hand, a frequency locking occurs between the rotation of the sphere around itself at an angular velocity, say  $\langle \dot{\phi} \rangle$ , and  $\omega_0$  :  $\langle \dot{\phi} \rangle \sim \omega_0$  (For this qualitative argument, there would be no need to define precisely  $\dot{\phi}$ , but a precise definition can be anyway given by looking at the definition of  $\phi$  in fig. 1). On the other hand, at large values of  $\omega_0$ , the effect of the magnetic field averages rapidly to zero, so the motion must converge to a free rolling (albeit constrained into a circular motion) for which the friction on the table, proportional to the coincidental point velocity  $\sim r_0 \dot{\alpha}_0 + R \dot{\phi}$ , is approximately zero. As a result, we have  $\dot{\alpha}_0 \sim -\omega_0 R / \langle r_0 \rangle \sim -\omega_0 (R / \ell_0)$ , for which in our case we have moreover  $R / \ell_0 \simeq 0.1$ . The other salient feature of the fig. 4 is its bell shape with a minimum around 16 Hz. This minimum signals a crossover between a complex regime with few large festoons which act as shortcuts during revolutions (and therefore enhance the absolute value of the revolution frequencies), and a second regime ( $\omega_0/2\pi > 16$  Hz) where the trajectories are close to circles, with many small festoons. For this regime, the previous arguments leading to  $\dot{\alpha}_0 \simeq \omega_0$  apply and explain the enhancement of  $|\dot{\alpha}_0|$ .

#### IV. MODELLING

To achieve a comprehensive description of the bead motion in the counter-rotative regime, we develop a detailed theoretical model that we solve numerically.

Let us term  $\Omega_0$  the rotation vector of the bead in the laboratory frame. We have for the time derivative in this frame  $d\mathbf{n}/dt = \Omega_0 \times \mathbf{n}$  which implies that  $\Omega_0 = \mathbf{n} \times (d\mathbf{n}/dt) + \dot{\psi}_0 \mathbf{n}$  where  $\dot{\psi}_0$  is the rotation velocity of the bead around its magnetic axis  $\mathbf{n}$ .

The location of the center of the sphere is given by the cylindrical coordinates  $(r_0, \alpha_0, z_0 = R)$ , such that the velocity of its center of mass is  $\mathbf{v}_G = \dot{r}_0 \mathbf{u}_r + r_0 \dot{\alpha}_0 \mathbf{u}_\alpha$ . From the Koenig's theorem, we get a unconstrained Lagrangian

$$\mathcal{L}_{\text{uncstr.}}(\mathbf{n}, r_0, \alpha_0, \dot{\mathbf{n}}, \dot{r}_0, \dot{\alpha}_0, \dot{\psi}_0, t) = \frac{m}{2} [\dot{r}_0^2 + r_0^2 \dot{\alpha}_0^2] + \frac{1}{5} m R^2 \left( \left[ \frac{d\mathbf{n}}{dt} \right]^2 + \dot{\psi}_0^2 \right) + \mu \mathbf{n} \cdot \mathbf{B}(r_0, \alpha_0, t) \quad (1)$$

where we used the expression  $2mR^2/5$  for the iner-

tia moment of the sphere with respect to one di-

ameter. Notice that the constraint  $\mathbf{n}^2 = 1$  affects the vector  $\mathbf{n}$  for all times, so that the actual Lagrangian which describes the frictionless dynamics is  $\mathcal{L} = \mathcal{L}_{\text{unestr}} - \frac{1}{2}\Lambda(t)\mathbf{n}^2$ , the function  $\Lambda(t)$  being the Lagrange multiplier associated to this constraint.

The dynamics of the sphere is affected by a possible friction of the sphere on the table (it is not constrained to roll only). This friction is modelled by a force  $\mathbf{F}_{\text{fr}}$  proportional to the velocity  $\mathbf{V}_0$  of the coincidental point  $I$  (the point of the sphere in contact with the table at any instant) :

$$\mathbf{F}_{\text{fr}} = -m\gamma\mathbf{V}_0 = -m\gamma(\mathbf{v}_G - R\boldsymbol{\Omega}_0 \times \mathbf{e}_z) \quad (2)$$

This friction can be incorporated in a Lagrangian description by means of the so-called Raileygh function

$$\mathcal{F} = \frac{m}{2}\gamma\mathbf{V}_0^2 \quad (3)$$

which modifies the Lagrange equations to

$$\frac{d}{dt} \frac{\partial \mathcal{L}}{\partial \dot{q}} = \frac{\partial \mathcal{L}}{\partial q} - \frac{\partial \mathcal{F}}{\partial \dot{q}} \quad (4)$$

for all variables  $q$  describing the dynamics.

The lengths are made dimensionless by defining  $\mathbf{r} = \mathbf{r}_0/\ell$  where  $\ell$  is a characteristic length of the rotating magnet (we will choose  $\ell$  slightly different from the actual length of the magnet  $\ell_m$ , as explained below). The magnetic field is also normalized according to  $\mathbf{B} = \mathbf{B}/B_0$  ( $B_0$  a characteristic magnetic field intensity of the rotating magnet). One defines  $\varepsilon = R/\ell$  and  $\kappa = B_0\mu/[mR^2\gamma^2]$ . This last constant can be interpreted as the square of the characteristic time of friction times the magnetic pulsation  $\sqrt{\mu B_0/mR^2}$ . A small value of  $\kappa$  means that friction will likely overdamp the oscillations caused by  $\mathbf{B}$  and its time evolution. Finally the time is normalized by  $t \leftarrow \gamma t$ . The outcome of these generalized dissipative and nondimensionalized Lagrange equations for  $q \in \{\mathbf{n}, \dot{\psi} = \gamma^{-1}\dot{\psi}_0, r, \alpha = \alpha_0\}$  is

$$\boldsymbol{\Omega} = \gamma^{-1}\boldsymbol{\Omega}_0 = \mathbf{n} \times \frac{d\mathbf{n}}{dt} + \dot{\psi}\mathbf{n}, \quad (5)$$

$$\mathbf{V} = (\ell\gamma)^{-1}\mathbf{V}_0 = \dot{r}\mathbf{e}_r + r\dot{\alpha}\mathbf{e}_\alpha - \varepsilon\boldsymbol{\Omega} \times \mathbf{e}_z, \quad (6)$$

$$\ddot{\mathbf{n}} = -(\dot{\mathbf{n}})^2\mathbf{n} - \frac{5}{2\varepsilon}(\mathbf{V} \times \mathbf{e}_z) \times \mathbf{n} + \frac{5\kappa}{2}[\mathbf{B} - \mathbf{n}(\mathbf{n} \cdot \mathbf{B})], \quad (7)$$

$$\ddot{\psi} = -\frac{5}{2\varepsilon}\mathbf{V} \cdot (\mathbf{e}_z \times \mathbf{n}), \quad (8)$$

$$\ddot{r} = r\dot{\alpha}^2 + \kappa\varepsilon^2\mathbf{n} \cdot \frac{\partial \mathbf{B}}{\partial r} - \mathbf{V} \cdot \mathbf{e}_r, \quad (9)$$

$$\frac{d(r^2\dot{\alpha})}{dt} = \kappa\varepsilon^2\mathbf{n} \cdot \frac{\partial \mathbf{B}}{\partial \alpha} - r\mathbf{V} \cdot \mathbf{e}_\alpha. \quad (10)$$

Notice that the derivative of  $\mathbf{B}$  with respect to  $\alpha$  includes the derivative of the unit vectors  $(\mathbf{e}_r, \mathbf{e}_\alpha)$  as

well as that of the coordinates  $(B_r, B_\alpha, B_z)$  in case of a representation with cylindrical coordinates.

To model the magnetic field created by the rectangular rotating magnet, we assume it can be described by five parallel and equidistant lines of magnetic dipoles characterized by a constant dipolar line-density  $d\mathcal{M}/dx'$  and a length  $2\ell$ . Their length  $\ell$  is close to  $\ell_m$ , but is adjusted so that the two maxima of the magnetic field on the plate are separated by the same distance (41 mm) in the experiment and the modelling. We found  $\ell = 0.82\ell_m = 23$  mm. On the other side, the distance between the two extremal lines are fixed to be exactly at  $w_m$  - the width of the actual magnet. The actual portrait of the magnetic field experienced by the bead in shown in fig. 5. The field created at the location  $\mathbf{r}_0 = (x_0, y_0, R)$  by a single magnetic line of length  $2\ell_0$ , directed along the horizontal unit vector  $\mathbf{e}'_x$ , and symmetrical with respect to the point  $(0, 0, -h_w)$  is:

$$\mathbf{B}(\mathbf{r}_0, t) = B_0 \left[ \frac{\mathbf{r}_0/\ell + (h_0/\ell)\mathbf{e}_z - s\mathbf{e}'_x(t)}{|\mathbf{r}_0/\ell + (h_0/\ell)\mathbf{e}_z - s\mathbf{e}'_x(t)|^3} \right]_{s=-1}^{s=+1} \quad (11)$$

where  $B_0 = \frac{\mu_0}{4\pi\ell^2} \frac{d\mathcal{M}}{dx'}$  and  $h_0 = h_w + R$ . The normalized version  $\mathbf{B}$  of this field is straightforwardly obtained by dividing by  $B_0$  and writing the right hand side in terms of  $\mathbf{r} = \mathbf{r}_0/\ell$  and  $h = h_0/\ell$ . The time dependence of the magnetic field is entirely borne by the vector  $\mathbf{e}'_x$  which rotates counterclockwise in the laboratory frame  $(O, \mathbf{e}_x, \mathbf{e}_y) : \mathbf{e}'_x(t) = \cos(\omega t)\mathbf{e}_x + \sin(\omega t)\mathbf{e}_y$ . Similarly the  $(r, \alpha)$  dependence is given by the term  $\mathbf{r} = r\mathbf{e}_r = r[\cos\Phi\mathbf{e}'_x + \sin\Phi\mathbf{e}'_y]$  with  $\Phi = \alpha - \omega t$ , see fig. 1.

### A. Numerical simulations results

We simulated the dynamics of the bead embodied by equations (7-10) using local spherical coordinates to represent  $\mathbf{n}$ , namely  $\mathbf{n} = \cos\theta\mathbf{e}_r + \sin\theta(\sin\phi\mathbf{e}_\alpha - \cos\phi\mathbf{e}_z)$ . The dynamical equations in these coordinates are given in appendix . To compare quantitatively experiments and simulations, we have to fix the values of the parameters  $\varepsilon$ ,  $\kappa$  and  $\gamma$ , the latter being involved in dimensionless angular velocities  $\omega = \omega_0/\gamma$  and  $\dot{\alpha} = \dot{\alpha}_0/\gamma$  for instance .  $\varepsilon$  is an imposed geometric parameter :  $\varepsilon = R/\ell = 0.11$ . The other two are rather difficult to determine from experiments, all the more so the actual friction within the experiment is a solid friction, in contrast with our modeling of a linear viscous one. As a result, we chose to adjust  $\kappa$  and  $\gamma$  so as to fit the experimental result at best. We found  $\kappa = 1.5$  and  $\gamma = 312.5 \text{ s}^{-1}$ . It gives a value  $\mu B_0 \sim 4.10^{-4} \text{ J}$ . For a typical neodymium bead, we have  $\mu \sim R^3 \times BH_{\text{max}}/B_{\text{rem}}$ , where  $BH_{\text{max}} \sim 10^5 \text{ J}\cdot\text{m}^{-3}$  is the maximum energy product and  $B_{\text{rem}} \sim 1 \text{ T}$

## V. ANALYSIS OF MOTION

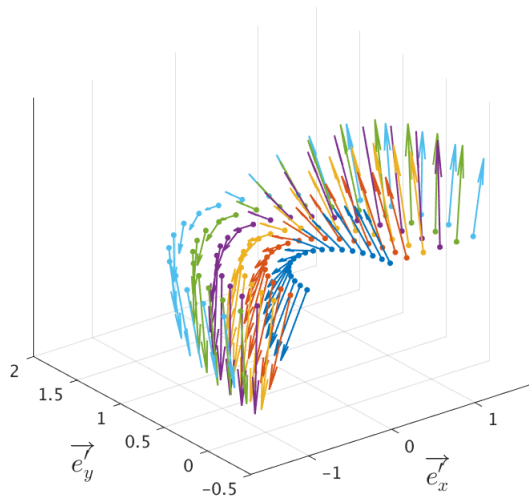


FIG. 5. Magnetic field generated by five magnetic lines parallel to  $\vec{e}'_x$ , of normalized length 1, regularly placed at  $y = n\lambda, n \in \{-2 : 2\}$ , with  $\lambda = w_m/(4\ell) = 0.435$ .

the remanence. We get here  $\mu \sim 10^{-2} \text{ A}\cdot\text{m}^{-1}$  and  $B_0 \sim 10^{-2} \text{ T}$ .

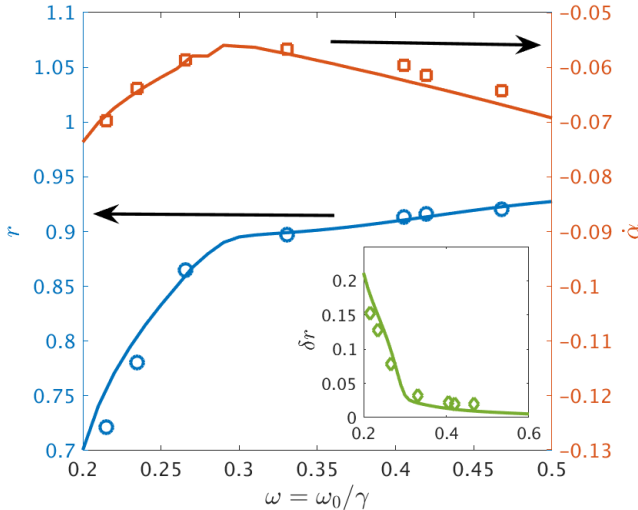


FIG. 6. Comparison between experiments (symbols) and simulation (solid lines). Left ordinate and blue circles : Mean normalized radius  $\langle r \rangle$ . Right ordinate and red squares : Mean normalized bead angular velocity  $\langle \dot{\alpha} \rangle$ . Inset : Standard deviation  $\delta r = [\langle r^2 \rangle - \langle r \rangle^2]^{1/2}$  vs.  $\omega$ .

With these values the agreement between experiment and simulations is quite quantitative, as can be seen in fig. 6.

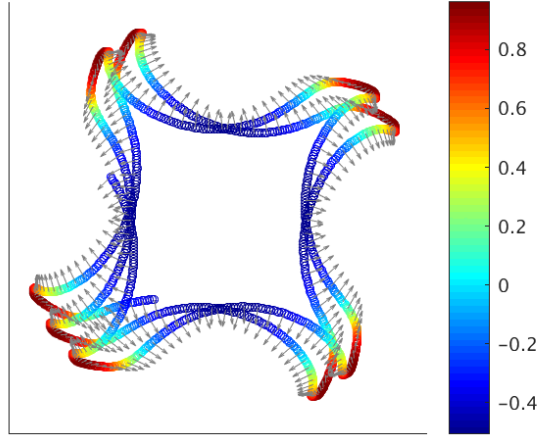


FIG. 7. Simulation for the frequency  $\omega = 0.215$  corresponding to the experiment of fig. 2. The color codes for the intensity of  $n_z$  and the arrows show the direction and the relative length of the horizontal component of  $\mathbf{n}$ .

### A. 4-fold counter-rotation

The advantage of numerical simulations is to provide easily the internal rotation of the bead. We first analyse the case represented in fig. 2 corresponding to  $\omega = 0.215$ . In fig. 7, the simulated trajectory is represented with a color code corresponding to the values of  $n_z \in [-1, 1]$ . Small gray arrows are also added to see the direction and relative length of  $\mathbf{n} - n_z \mathbf{e}_z$ . It is worth noting that the mean value of  $n_z$  is not zero, which indicates that a different, conjugate solution at this frequency exists where polarities of  $\mathbf{n}$  and  $\mathbf{B}$  are simultaneously reversed. In this case the corners of the square-like shape of the trajectories would correspond to minima  $n_z \simeq -1$ . It is worth mentioning that in this motion, the bead's moment stays remarkably parallel to the magnet field, as can be seen in the fig. 8 (top) : Their relative angle does not exceed 4 degrees. The bottom plot shows the magnitude of the coincidental velocity. It can be seen that the high friction zones are tightly correlated to those (rare) moments where the bead axis cannot follow the rate of variation of the magnet's field. It is also interesting to note that the magnitude of the magnetic field experienced by the bead during its revolution does not vary more than 13% with respect to its mean value (not shown).

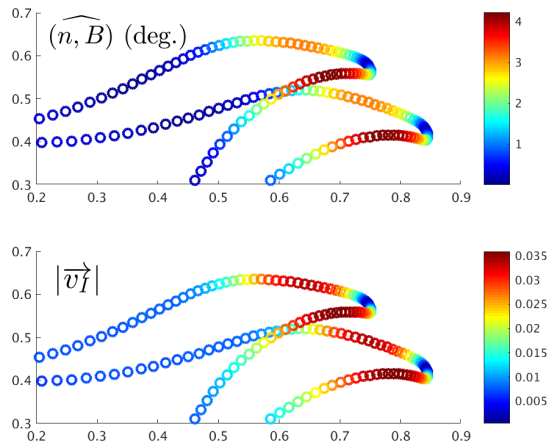


FIG. 8. Same as fig. 7 (upper right corner only), the color codes showing in the top plot the angle between the magnetic axis of the bead and the local magnetic field (in degrees), and in the bottom plot the magnitude of the co-incident point velocity, proportional to the friction force experienced by the bead.

### B. Many-fold counter-rotation

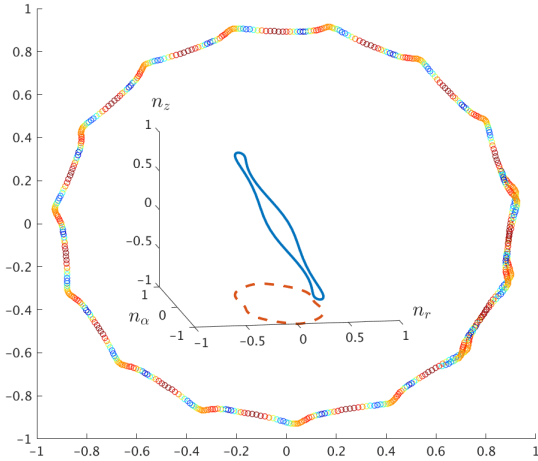


FIG. 9. Trajectory of the magnetic bead for  $\omega = 0.4$ . The color modulates according to the magnitude of the friction frequency. The inset (solid blue line) shows the closed trajectory of the vector  $\mathbf{n}$  in the local coordinate frame  $(\mathbf{e}_r, \mathbf{e}_\alpha, \mathbf{e}_z)$ .

For increasing values of  $\omega$ , the counter-rotation tends to adopt a more circular shape, as can be seen from fig. 9. The festoons are numerous (15 for  $\omega = 0.4$ ) and have a small amplitude. As before, the magnetic bead stays remarkably parallel to the local

magnetic field (the angle is never larger than  $3^\circ$ ), and in the local frame  $(\mathbf{e}_r, \mathbf{e}_\alpha, \mathbf{e}_z)$ , the trajectory is closed and almost circular, with the magnetic moment vector displaying a mild tilt ( $\simeq 25^\circ$ ) with respect to the vertical.

### VI. TIME AVERAGINGS

The full dynamical behaviour of the bead is complicated and certainly non integrable.

One can nevertheless try to make some predictions concerning the mean radius of counter-rotation and the associated rotation frequency, at least in the regime where  $r$  stays reasonably constant.

The map of the field shows that close to the maximum, it has essentially an (slightly tilted) orthoradial structure. It is thus reasonable to assume that in the dynamical regimes where  $r \simeq 1$ , one can neglect the radial dependence of  $\mathbf{n}$ , assume  $\theta \simeq \pi/2$  and write  $\mathbf{n} \simeq \sin \phi \mathbf{e}_\alpha - \cos \phi \mathbf{e}_z$ . Likewise, we neglect also the fluctuations in  $r$  and  $\dot{\alpha}$ . Writing again  $r$  and  $\dot{\alpha}$  for the temporal averages  $\langle r \rangle$  and  $\langle \dot{\alpha} \rangle$ , we have

$$0 = r\dot{\alpha}^2 + \kappa\varepsilon^2 \partial_r \langle B_\alpha \sin \phi - B_z \cos \phi \rangle - \langle \mathcal{V}_r \rangle, \quad (12)$$

$$0 = \kappa\varepsilon^2 \langle [\partial_\alpha B_\alpha + B_r] \sin \phi - \partial_\alpha B_z \cos \phi \rangle - r \langle \mathcal{V}_\alpha \rangle, \quad (13)$$

$$0 = \kappa\varepsilon \langle B_\alpha \cos \phi + B_z \sin \phi \rangle - \langle \mathcal{V}_\alpha \rangle. \quad (14)$$

In the approximation considered, one has, from the formula (24) of the Appendix,  $\mathcal{V}_\alpha \simeq r\dot{\alpha} + \varepsilon\dot{\phi}$ . The

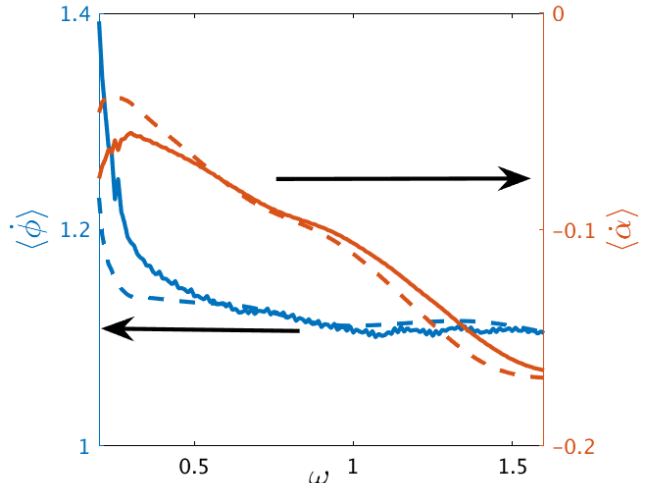


FIG. 10. Test of the formulas (15) : The solid lines show  $\langle \phi \rangle$  (blue, left ordinate) and  $\langle \dot{\alpha} \rangle$  (red, right ordinate) and the dashed show the result of (15).

equation (12) shows that the centrifugal force is counterbalanced by a magnetic force only if  $\phi$  oscillates

with the same frequency as  $\Phi = \alpha - \omega t$ . This leads us to assume  $\phi = -\Phi + \chi$  where  $\chi$  is a constant phase. One can show (but the calculation is cumbersome) that the averages implying the magnetic field in eqs (13) and (14) are all  $\propto \sin(\chi)$  for symmetry reasons, whereas that of (12) is  $\propto \cos(\chi)$ . The solution of these equations is therefore somewhat simplified, since they reduce to (i)  $\chi \equiv 0$  modulo  $\pi$  and (ii)  $\langle \mathcal{V}_\alpha \rangle = 0$  and (iii) eq. (12). Actually, one can guess in advance that the phase locks to  $\chi = \pi$ , because it corresponds to the most stable situation where the bead visits the region of maximum magnetic field in the orientation which minimizes the magnetic energy interaction. Combining  $\dot{\phi} = \omega - \dot{\alpha}$  and  $r\dot{\alpha} + \varepsilon\dot{\phi} = 0$ , we obtain

$$\dot{\alpha} = -\frac{\varepsilon\omega}{r - \varepsilon} \text{ and } \dot{\phi} = \frac{\omega r}{r - \varepsilon}. \quad (15)$$

The comparison of these formulas with the actual averages of  $\dot{\phi}$  and  $\dot{\alpha}$  are shown in fig. 10 and the result is convincing for  $\omega \geq 0.5$ , that is for frequencies higher than those obtained in the experiments of fig. 6. This means that the hypothesis of free rolling corresponding to the relation  $r\dot{\alpha} + \varepsilon\dot{\phi} = 0$  is quantitatively correct only at quite large frequencies. Regarding the prediction for the mean value of  $r$ , one would use eq. (12), but this equation would be tractable only if  $\langle \mathcal{V}_r \rangle$  is negligible with respect to the other terms, since the expression (23) for  $\mathcal{V}_r$  contains a term  $-\varepsilon\psi \sin \theta \sin \phi$  addressing directly the rotation of the bead around its magnetic axis, a motion that is coupled to all degrees of freedom. As can be seen from the inspection of

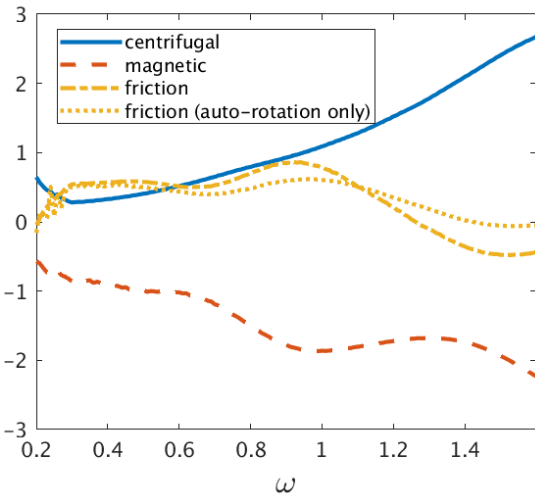


FIG. 11. Evolution with  $\omega$  of the three terms of eq. (12). “centrifugal” refers to  $r\dot{\alpha}^2$ , “magnetic” to  $\kappa\varepsilon^2\partial_r\langle B_\alpha \sin \phi - B_z \cos \phi \rangle$  and “friction” to  $-\langle \mathcal{V}_r \rangle$ . The dotted yellow curve shows  $\varepsilon\langle \psi \sin \theta \sin \phi \rangle$ , the term of  $-\langle \mathcal{V}_r \rangle$  depending on the rotation of the bead around its magnetic axis. All curves are divided by  $\varepsilon^2$ .

fig. 11, the friction term  $-\langle \mathcal{V}_r \rangle$  is not at all negligible

in the regime  $\omega < 0.5$  and becomes negligible with respect to the other two only at quite higher frequencies. As a result, one concludes that the quantitative features of the counter-rotating regime cannot be simply obtained in the moderate driving frequencies where the festooning of the trajectories is marked.

A final comment can be made about an implicit choice made in assuming  $\phi = -\Phi + \chi$ , a relation dictated by the requirement that  $\phi$  and  $\Phi$  must lead to resonant terms in the magnetic force. There is here an implicit because  $\phi = \Phi + \chi$  would have been also a valid choice. In Appendix IX B it is shown why this Ansatz, which would give a co-rotative regime, is actually never observed.

### A. Physical origin of the festoons

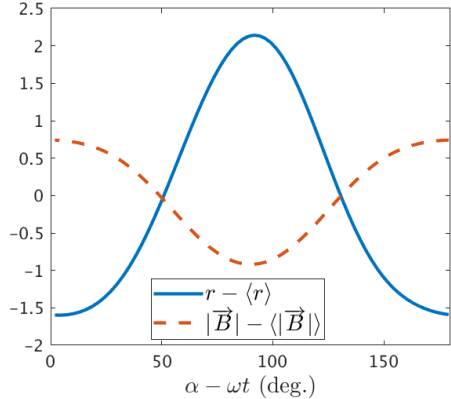


FIG. 12. Fluctuations of  $r$  (solid blue) and  $|\mathbf{B}|$  (dashed red) during half a revolution of the magnet. The abscissa is the angle between the bead and the rotating magnet. Notice that when the magnet and the bead are on top of each other, the value of  $r$  is minimal and is 0.89, i.e. the location of the maximum of the field.

On the qualitative level, the origin of the festoons can be understood if one realizes that the magnetic axis of the bead stays always nearly colinear to the local magnetic field. As a result, the effective magnetic force for the bead’s center of mass is high near the ends of the magnet where the field varies substantially over a short distance. As shown in fig. 12, one sees that the radius is minimal, around 0.89 (the location of the absolute maximum of field), when the magnet crosses the bead angular position. When the magnet axis goes away from the bead angular position, the field variations weaken, the centrifugal force “wins” and drives the bead away from  $r = 0.89$ , whence the maximum of  $r$  at precisely  $\alpha - \omega t = \pi/2$ . However, the detailed shape of the festoons cannot be accounted for by such a simple force balance argument, because in the vicinity of the maxima of  $r$ , the friction force is

no longer negligible in the budget, as can be seen in fig. 8 (bottom).

## B. Paramagnetic bead

As correctly noticed in [11], the mechanism for the counter-rotation proposed by [7] relies on the presence of a remanent magnetization in the beads, and the counter-rotation observed with steel beads would be entirely due to it. With the theory presented in this work and summarized by equations (5-10), it is possible to test an ideal case where the magnetic interaction would be solely paramagnetic. It amounts to replacing the interaction potential in the Lagrangian by  $V = -\alpha_m B^2$ . The most important consequence of this new interaction is that the rotational dynamics of the bead is now decoupled from the magnetic field by direct interaction, that is the term  $\propto \kappa$  in (7) disappears. All the arguments put forth previously to account for the counter-rotation are no longer valid, and we indeed never observed counter-rotation in simulations of the purely paramagnetic bead.

But it is even possible to show that in the limit of large  $\omega$ , a counter-rotating stationary motion is impossible. To do so, we multiply the equation (9) (with a magnetic term now  $-\partial_r V = \alpha_m \partial B^2 / \partial r$ ) by  $\dot{r}$  and (10) (same remark with  $-\partial_\alpha V$ ) by  $\dot{\alpha}$ , then add the two and take the time average. We get

$$0 = \alpha_m \left\langle \dot{r} \frac{\partial B^2}{\partial r} + \dot{\alpha} \frac{\partial B^2}{\partial \alpha} \right\rangle - \langle \dot{r} \mathcal{V}_r + r \dot{\alpha} \mathcal{V}_\alpha \rangle \quad (16)$$

$$= \alpha_m \omega \left\langle \frac{\partial B^2}{\partial \alpha} \right\rangle - \langle \dot{r} \mathcal{V}_r + r \dot{\alpha} \mathcal{V}_\alpha \rangle \quad (17)$$

where we used the relation  $\partial B^2 / \partial t = -\omega \partial B^2 / \partial \alpha$  in the last expression. The equation (10) shows moreover that  $\alpha_m \langle \partial B^2 / \partial \alpha \rangle = \langle r \mathcal{V}_\alpha \rangle$ . On the other hand, the evolution of the energy function [14]  $h = \dot{q} \partial \mathcal{L} / \partial \dot{q} - \mathcal{L}$  is  $dh/dt = -2\mathcal{F} - \partial \mathcal{L} / \partial t$  which yields

$$\langle \mathcal{V}_r^2 + \mathcal{V}_\alpha^2 \rangle = \alpha_m \omega \left\langle \frac{\partial B^2}{\partial \alpha} \right\rangle \quad (18)$$

On comparing (17) and (18), and writing  $\mathcal{V}_r = \dot{r} + \hat{\mathcal{V}}_r$  and  $\mathcal{V}_\alpha = r \dot{\alpha} + \hat{\mathcal{V}}_\alpha$ , we see that we have exactly

$$\langle \mathcal{V}_r \hat{\mathcal{V}}_r + \mathcal{V}_\alpha \hat{\mathcal{V}}_\alpha \rangle = 0 \quad (19)$$

Now we make use of the hypothese  $\omega \rightarrow \infty$  and assume that in this asymptotic limit, a quasi-free rolling is at work, since the magnetic field varies extremely rapidly and averages to zero. We describe this free rolling by assuming  $\theta \simeq 0$ , i.e. the axis of rotation is precisely  $\mathbf{n}$  and is of course along  $\mathbf{e}_r$  (we remind that the material axis  $\mathbf{n}$  can be chosen arbitrarily for a paramagnetic bead). With this assumption, we have that

(see formulas (23) and (24))  $\hat{\mathcal{V}}_r \simeq 0$  and  $\hat{\mathcal{V}}_\alpha \simeq \varepsilon \dot{\psi}$ , from which and (19) we conclude that  $\langle \mathcal{V}_\alpha \hat{\mathcal{V}}_\alpha \rangle = 0$ . We can therefore rewrite (17) as

$$0 = \omega \langle r \mathcal{V}_\alpha \rangle - \langle (\dot{r})^2 + \mathcal{V}_\alpha^2 \rangle \quad (20)$$

With a small error (since for  $\omega \rightarrow \infty$ , the fluctuations of  $\dot{\alpha}$  are small), we can change this relation to

$$0 = \frac{\omega}{\langle \dot{\alpha} \rangle} \langle r \dot{\alpha} \mathcal{V}_\alpha \rangle - \langle \dot{r}^2 + \mathcal{V}_\alpha^2 \rangle \quad (21)$$

$$= \left( 1 - \frac{\omega}{\langle \dot{\alpha} \rangle} \right) \langle \mathcal{V}_\alpha^2 \rangle + \langle \dot{r}^2 \rangle \quad (22)$$

This relation shows that  $\langle \dot{\alpha} \rangle$  and  $\omega$  cannot have opposite signs : the counter-rotation is impossible in the limit of large  $\omega$  for purely paramagnetic beads.

## VII. CONCLUSION

In this paper, we have presented a coherent study of the counter-rotation of a ferromagnetic bead, constrained to move on a magnetic stirrer's surface, and excited by the rotation at constant angular velocity of the magnet installed beneath the slab of the stirrer. By fitting two parameters, we were able to reproduce quantitatively by numerical simulations the experimental observations, first observed by [11] in a very similar experiment, in spite of the different type of friction of the bead on the slab utilized (viscous vs. dry friction). The expression of the dynamical equations of the ten degrees of freedom of the problem (two for the bead's center of mass, three for the orientation of the bead, plus the same number for their time derivatives), allowed us to make also some theoretical analysis in the regime of high frequencies. We show in particular that the corotative regime is never stable at high frequencies (whereas it would be observable for a system of a magnetic disk holonomically constrained to roll at a fixed distance from the center) and furthermore that a purely paramagnetic and isotropic bead can never display counter-rotation. Therefore the slow counter-rotation observed by [11] with steel spheres are entirely attributable to the slight remanent magnetization or magnetic anisotropy of the spheres. We further analyzed the dynamical behavior of the bead when festoons are present and showed that the associated modulation of the radial distance of the bead is tightly correlated to—and therefore mainly due to—the modulation of the radial component of the magnetic force : When this component weakens, the centrifugal force moves the bead away from the rotation center, and conversely. This simple argument is asymptotically true only for  $\omega \rightarrow \infty$ . At lower frequencies, the friction force is not negligible, cf. fig. 11. We noted that the proper asymptotic regime would be

experimentally difficult to obtain since it corresponds to frequencies  $\sim 10^2$  Hz.

This study can be pursued in several interesting ways : What happens when the bead is constrained to move in a fluid or on a fluid surface, and is likely to be sensitive to the waves generated by itself ? Recent studies have shown the extraordinary behaviors which happen in such composite systems of a bead or droplet and an interacting fluid, when the latter has a long relaxation time [8, 10, 15]. Another interesting question would be to probe the behaviour of non spherical magnets : As the asymptotic ( $\omega \rightarrow \infty$ ) is a free rolling for the sphere, how does a non spherical magnet accommodate to high excitation frequencies ? Finally, a third class of follow-ups would be to inquire the collective behaviour of several beads excited together by the magnetic stirrer. Such systems may display emergent properties, typical of dissipative-active systems, where a continuous flux of energy drives assemblies of particles far from equilibrium into a unexpected stationary and complex dynamical regimes.

### VIII. ACKNOWLEDGEMENTS

We thank numerous students who worked during their internship on this experiment or on variants of it : Elodie Adam, Vanessa Bach, Jérémie Geoffre, Vincent Hardel, Alexandre Ohier, Yona Schell and Camille Vandersteen Mauduit-Larive.

### IX. APPENDICES

#### A. Dynamical equations in spherical coordinates

For sake of completeness, we provide here the dynamical equations (Eq. (7)) for the magnet axis  $\mathbf{n}$  in the spherical coordinates defined by  $\mathbf{n} = \cos \theta \mathbf{e}_r + \sin \theta (\sin \phi \mathbf{e}_\alpha - \cos \phi \mathbf{e}_z)$  :

$$\begin{aligned} \mathcal{V}_r &= \dot{r} - \varepsilon \left( \dot{\theta} \cos \phi + \dot{\alpha} \sin^2 \theta \sin \phi \cos \phi \right. \\ &\quad \left. - \dot{\phi} \sin \theta \cos \theta \sin \phi + \dot{\psi} \sin \theta \sin \phi \right), \end{aligned} \quad (23)$$

$$\mathcal{V}_\alpha = r \dot{\alpha} + \varepsilon \left( \dot{\phi} \sin^2 \theta + \dot{\alpha} \sin \theta \cos \theta \cos \phi + \dot{\psi} \cos \theta \right). \quad (24)$$

$$\begin{aligned} \frac{d}{dt} \left[ \dot{\theta} + \dot{\alpha} \sin \phi \right] &= \dot{\phi}^2 \sin \theta \cos \theta + \dot{\alpha}^2 \sin \theta \cos \theta \sin^2 \phi \\ &+ \dot{\alpha} \dot{\phi} \cos(2\theta) \cos \phi + \frac{5\kappa}{2} \frac{\partial \mathbf{n}}{\partial \theta} \cdot \mathbf{B} + \frac{5}{2\varepsilon} \mathcal{V}_r \cos \phi, \end{aligned} \quad (25)$$

$$\begin{aligned} \frac{d}{dt} \left[ \dot{\phi} \sin^2 \theta + \dot{\alpha} \sin \theta \cos \theta \cos \phi \right] &= \dot{\alpha}^2 \sin^2 \theta \sin \phi \cos \phi \\ &+ \dot{\alpha} \dot{\theta} \cos \phi - \dot{\alpha} \dot{\phi} \sin \theta \cos \theta \sin \phi \\ &+ \frac{5\kappa}{2} \frac{\partial \mathbf{n}}{\partial \phi} \cdot \mathbf{B} - \frac{5\kappa}{2\varepsilon} [\mathcal{V}_r \sin \theta \cos \theta \sin \phi + \mathcal{V}_\alpha \sin^2 \theta]. \end{aligned} \quad (26)$$

$$\ddot{\psi} = \frac{5}{2\varepsilon} [\mathcal{V}_r \sin \theta \sin \phi - \mathcal{V}_\alpha \cos \theta]. \quad (27)$$

#### B. Why is rapid corotation never observed ?

In the preceding analysis, we found only a counter-rotating regime (i.e.  $\omega \dot{\alpha} < 0$ ) because we have assumed  $\phi = -\Phi + \chi = \omega t - \alpha + \chi$ . Another possibility to have a nonzero radial magnetic force resisting the centrifugal force would have been to write  $\phi = \Phi + \chi$ . In this case, we would find a corotative regime, with  $\dot{\alpha} = \varepsilon \omega / (r + \varepsilon)$  and  $\dot{\phi} = -\omega r / (r + \varepsilon)$ , and  $\chi = \pi$  because the stability criterion assumed above is obviously still valid. To understand why this corotative regime is observed neither in the experiments nor in the simulations, we assume for sake of simplicity that the driving frequency is so high that we can disregard the friction term  $\langle \mathcal{V}_r \rangle$  in (12). We also model the magnetic field experienced by the bead by the orthoradial structure  $\mathbf{B} \simeq \hat{B}(r)[\sin(\Phi)\mathbf{e}_\alpha + \cos(\Phi)\mathbf{e}_z]$  where  $\hat{B}(r)$  is the typical field amplitude along the trajectory at mean radius  $r$ . Notice that the trigonometric factors in this formula are dictated by the geometrical structure of the field, see fig. 5. The mean magnetic force resisting the centrifugal force is  $F_{\text{mag}} = \kappa \varepsilon^2 \partial_r \langle B_\alpha \sin \phi - B_z \cos \phi \rangle$ . With the counter-rotative Ansatz  $\phi = -\Phi + \pi$ , we have  $F_{\text{mag}} = \kappa \varepsilon^2 \partial_r \hat{B}(r)$ , which is negative (as required) for typical values of  $r$  larger than the value where  $\hat{B}(r)$  is maximum. With the corotative Ansatz  $\phi = \Phi + \pi$ , we would have  $F_{\text{mag}} = -\kappa \varepsilon^2 \partial_r \hat{B}(r) \langle \cos(2\Phi + \pi) \rangle = 0$ . In fact, this value is not strictly zero, since we made approximations concerning the structure of the field. However, it is small and therefore precludes the stabilization of a corotative motion.

---

[1] Dominic Vella, Emmanuel du Pontavice, Cameron L Hall, and Alain Goriely. The magneto-elastic: from self-buckling to self-assembly. *Proceedings of the Royal Society A: Mathematical, Physical and Engineering Sciences*, 470(2162):20130609, 2014.

[2] René Messina and Igor Stanković. Self-assembly of magnetic spheres in two dimensions: The relevance of onion-like structures. *EPL (Europhysics Letters)*, 110(4):46003, may 2015.

[3] Lydiane Becu, Marc Basler, Miodrag L. Kulić, and Igor M. Kulić. Resonant reshaping of colloidal clusters

on a current carrying wire. *The European Physical Journal E*, 40(12):107, 2017.

[4] Sándor Egri and Gábor Bihari. Self-assembly of magnetic spheres: a new experimental method and related theory. *Journal of Physics Communications*, 2(10):105003, 2018.

[5] Unpublished results.

[6] Pietro Tierno, Tom H. Johansen, and Thomas M. Fischer. Localized and delocalized motion of colloidal particles on a magnetic bubble lattice. *Phys. Rev. Lett.*, 99:038303, Jul 2007.

[7] Christophe Gissinger. Wave-induced motion of magnetic spheres. *EPL (Europhysics Letters)*, 112(5):50003, dec 2015.

[8] A. Snejhko, I. S. Aranson, and W.-K. Kwok. Surface wave assisted self-assembly of multidomain magnetic structures. *Phys. Rev. Lett.*, 96:078701, Feb 2006.

[9] Bartosz A Grzybowski, Howard A Stone, and George M Whitesides. Dynamic self-assembly of magnetized, millimetre-sized objects rotating at a liquid-air interface. *Nature*, 405(6790):1033–1036, 2000.

[10] James E. Martin and Alexey Snejhko. Driving self-assembly and emergent dynamics in colloidal suspensions by time-dependent magnetic fields. *Reports on Progress in Physics*, 76(12):126601, December 2013.

[11] Yeung Yeung Chau, Ruo-Yang Zhang, and Weijia Wen. Reverse rotation of soft ferromagnetic ball in rotating magnetic field. *Journal of Magnetism and Magnetic Materials*, 476:376–381, 2019.

[12] Blender Online Community. *Blender - a 3D modelling and rendering package*. Blender Foundation, Stichting Blender Foundation, Amsterdam, 2018.

[13] As remarked in [11], these festoons are locally similar to the family of mathematical curves named trochoids, or more precisely to hypocycloids, which are constructed as the locus of a point of a disk rolling inside and against another, larger one.

[14] Herbert Goldstein. *Classical Mechanics*. Addison-Wesley, 1980.

[15] Yves Couder and Emmanuel Fort. Single-particle diffraction and interference at a macroscopic scale. *Phys. Rev. Lett.*, 97:154101, Oct 2006.